29th AIAA Applied Aerodynamics Conference **AIAA 2011-3971**
27 - 30 June 2011, Honolulu, Hawaii

Multi-Element Airfoil Configurations for Wind Turbines

Adam M. Ragheb* and Michael S. Selig†
University of Illinois at Urbana-Champaign, Department of Aerospace Engineering, Urbana, IL 61801

The extremely thick blade root airfoils of the modern megawatt-scale wind turbines are prone to having sharp stall characteristics with associated unsteady aerodynamic blade loading and fatigue. With current technology designs reaching 45% thickness, these thick airfoils are incapable of producing high lift, and as a consequence they are aerodynamically and structurally sub-optimal. A computational study investigated candidate multi-element airfoil configurations that would serve as an aerodynamic fairing for an assumed spar cap geometry based on the DU 00-W-401 blade root airfoil geometry. Seven multi-element airfoil configurations with varying combinations of flaps, slats, and struts were developed and refined using an inviscid multipoint inverse airfoil design method. The airfoil configurations were then analyzed at Reynolds numbers typical of a utility-scale wind turbine. All of these configurations demonstrated the capability to produce significantly higher lift-to-drag ratios and lift coefficients than the baseline DU 00-W-401 airfoil, with $C_l/C_{d_{max}}$ increases of up to 82%. In addition to this performance increase, some of the configurations demonstrated a significantly gentler fall off in C_l/C_d at angles of attack greater than $\alpha_{C_l/C_{d_{max}}}$. In addition to the higher lift-to-drag ratios and lift coefficients, these multi-element configurations are expected to offer better start-up performance due to higher start-up torque and also higher blade efficiency from more closely matched ideal operating conditions.

Nomenclature

C_l	=	lift coefficient
$C_{l_{max}}$	=	maximum lift coefficient
C_l/C_d	=	lift-to-drag ratio
$C_l/C_{d_{max}}$	=	maximum lift-to-drag ratio
Re	=	Reynolds number
t/c	=	thickness-to-chord ratio
x/c	=	position-to-chord ratio
α	=	angle of attack relative to the defined chord line
$\alpha_{C_l/C_{d_{max}}}$	=	angle of attack for $C_l/C_{d_{max}}$

I. Introduction

The goal of this study was to develop concept multi-element airfoil configurations designed to increase the aerodynamic performance of the inboard section of a wind turbine blade. In addition to improving the blade aerodynamics, the motivations behind this study were threefold: lowering the cut-in wind speed, improving transportability of large wind turbine blades, and creating the ability to increase the spar cap separation to allow for structural optimization of the blades. Modern utility-scale wind turbines (1.5 – 10 MW rated power) have cut-in wind speeds between 3 and 5 m/s and do not begin to operate at their rated power until wind speeds of between 10 and 15 m/s are achieved. Increasing the lift coefficient of the inboard section of a wind turbine blade will aid in starting the wind turbine at lower speeds and will allow the turbine to produce its rated power at a lower wind speed. These improvements would in turn increase the power output, increase the capacity factor, and open up new locations for wind turbines that would otherwise be unsuitable for wind turbine placement.

In regards to transportation, current wind turbine blades appear to have reached the maximum size that can be easily transported. Constructing a longer or thicker root section may render the blade incompatible with current transportation

*Graduate Research Assistant, AIAA Student Member.
†Associate Professor, AIAA Senior Member.

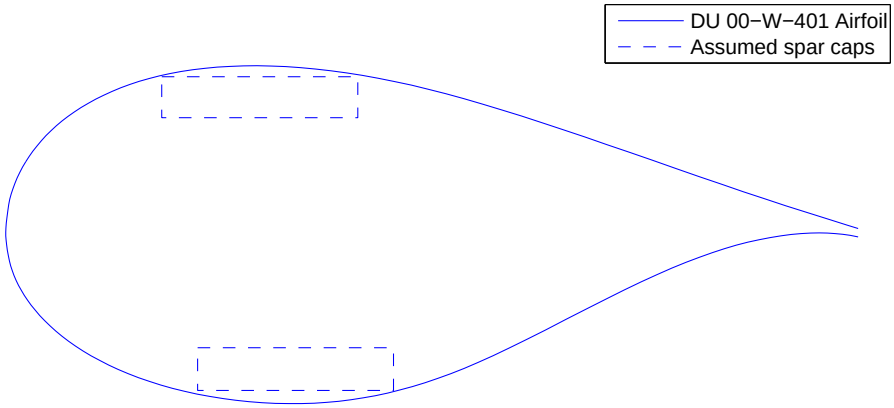

Figure 1. DU 00-W-401 airfoil and concept spar cap geometry.

infrastructure. The most substantial limit in the design of utility-scale is the transportation cost, which grows rapidly for lengths of over 46m and reaches prohibitive levels for blades over 61m long.[1] Multi-element configurations may allow for natural disconnect points on the blades, allowing the root section to be disassembled from the rest of the blade and the components to be transported to the wind farm site for assembly. These natural disconnect points will result in a simplification of the transportation process for a given blade radius or the ability to transport blades of larger radii.

The third and final motivation of this study was structural optimization of the wind turbine blades. With current blade root airfoils approaching 45% thickness, increasing the thickness and hence spar cap depth is aerodynamically undesirable and is not feasible because these airfoils are already aerodynamically inferior. Multi-element airfoil configurations may be tailored to facilitate even greater spar cap separations that could greatly improve the structural efficiency of the next generation of multi-megawatt wind turbines.

An inviscid multipoint inverse airfoil design method was used to develop and refine the multi-element configurations in this research. The PROFOIL[2–4] code with the MFOIL graphical user interface was used to develop the configurations and to fine tune the velocity distributions. The velocity distributions were prescribed in order to mitigate adverse pressure gradients which would be expected to lead to separation in an experimental or inviscid computational investigation. The use of the MFOIL user interface allows changes to the structural constraints to be easily and rapidly incorporated into the multi-element design. The relocation of a spar cap or the addition of a rear spar would not preclude the user from achieving significantly better aerodynamic results when compared with existing thick blade root airfoils, allowing significantly more freedom in the structural design of the blade.

The multi-element configurations were also analyzed using the multi-element airfoil analysis program MSES.[5–7] The aerodynamic performance of the multi-element configurations was investigated at Reynolds numbers encountered on utility-scale wind turbines, and the results were used to iterate on the designs. An emphasis was placed on the lift-to-drag ratios, and the behavior of C_l/C_d beyond $C_l/C_{d_{max}}$. MSES solves the steady Euler equations with a finite volume method on an "intrinsic streamline grid"[5] and was well-suited for this study due to its ability to solve partially-separated flows and its low computational cost.

Van Rooij and Timmer[8] stated that inboard wind turbine airfoil design can be primarily focused on structural demands and high lift due to the lack of roughness sensitivity in the root area. This lack of roughness sensitivity is a result of significant near-root rotational effects. For this reason, all multi-element airfoil configurations in this study were analyzed with natural transition.

II. Concept Spar Cap Geometry

For this study, the DU 00-W-401 airfoil geometry was used as a benchmark for gauging nominal spar cap spacing. Based on this geometry and prior wind turbine experience, the location and dimensions of the top and bottom spar caps were approximated. The DU 00-W-401 airfoil section with the concept spar cap geometry is shown in Fig. 1. The 40.1% thick DU 00-W-401 wind turbine root airfoil was reported to have a $C_{l_{max}}$ value of around 1.04 at $Re = 3.0 \times 10^6$ and $\alpha = 8.5$ deg.[8]

Based on the unit chord the nondimensional spar caps shown in Fig. 1 are 0.23×0.048, and they have a separation of 0.27. The front of the top spar cap is located at $x/c = 0.183$, and the front of the lower spar cap is located at $x/c = 0.225$. This concept spar cap geometry was oversized to add flexibility to the candidate multi-element configuration designs.

III. Multi-Element Airfoil Configurations

A total of seven multi-element airfoil configurations are presented. These configurations were designed with various combinations of slats, flaps, and struts arranged around a main airfoil element. In this study, the main airfoil element served as a fairing for the upper spar cap while the strut element faired the lower spar cap. Slats and flaps were located fore and aft of the main and/or strut elements, respectively. The entire arrangement was scaled to have a unit chord across the upper elements as shown by the dotted chord line in Fig. 2. This scaling was done in order to allow for a direct comparison of the airfoil and multi-element configuration lift coefficients.

The naming convention for all seven configurations uses letters to represent each of the separate elements. This naming convention is summarized in Table 1.

Table 1. Multi-Element Airfoil Naming Convention

Letter	Location	Element Represented
S	beginning	slat
M	any	main
F	any	flap
S	following any letter	strut

As an example, an *S* preceding an *M* represents a slat acting on the main element. An *F* following an *M* or *S* refers to a flap associated with a main or strut element preceding it. Following this convention, a configuration named SMFSF would have a main element with both a slat and flap acting on the main element in addition to a strut element with a flap acting on the strut.

The discussion of each arrangment includes four figures. The first figure depicts the multi-element airfoil geometry with the multi-element configuration chord line, the DU 00-W-401 airfoil,[8] and assumed spar caps coplotted. The second and third figures depict the flow properties across the multi-element configuration. The lefthand of this pair of figures shows the C_p distribution of the individual elements at $Re = 3.0 \times 10^6$ and $\alpha_{C_l/C_{d\,max}}$ as determined by MSES.[7] The righthand figure shows the nondimensional velocity distributions from MFOIL at the same α. The aforementioned two figures are located side-by-side. The fourth and final figure for each of the seven multi-element configurations compares the aerodynamic performance of each configuration to the DU 00-W-401 airfoil in MSES at $Re = 3.0 \times 10^6$. These four figures taken together demonstrate how the inviscid pressure distributions were designed and how the multi-element configurations performed around $C_l/C_{d_{max}}$. Additionally, these four figures demonstrate that the adverse pressure gradients were reasonable and no undesirable effects arose in the viscous case at the design point. As determined by MSES, the DU 00-W-401 airfoil at $Re = 3.0 \times 10^6$ has an $C_l/C_{d_{max}}$ of 82.9 at $C_l = 1.04$ and $\alpha = 6.5$ deg. These data along with that for each of the respective multi-element airfoils is given in Table 2 for later reference in the discussion to follow.

Table 2. Multi-Element Airfoil Performance Summary

Airfoil	$C_l/C_{d_{max}}$	C_l at $C_l/C_{d_{max}}$	% Increase in $C_l/C_{d_{max}}$
DU 00-W-401	82.9	1.04	–
MFS-004	152.9	2.42	84.4
MFS-104	156.1	2.42	88.3
MFFS-018	158.0	2.34	90.5
SMFS-004	150.4	2.82	81.4
MSS-001	116.9	1.77	41.0
MSS-102	121.1	2.01	46.1
MFSF-006	128.4	2.99	54.9

III.A. MFS-004: Main Airfoil Element, Flap, and Strut

The first case is named the MFS-004 and has a main element with a flap and a lower strut for the bottom spar cap located beneath the main-flap arrangement as shown in Fig. 2. The MFS-004 was the basis for all the arrangements, and produced a $C_l/C_{d_{max}} = 152.9$ at a $C_l = 2.42$ and $\alpha = 10$ deg. The main element of the MFS-004 was thicker than required to fair over the spar caps and thus is a rather conservative configuration. Figure 3 presents the viscous C_p and nondimensional velocity distributions at $C_l/C_{d_{max}}$. As shown by Fig. 3, the strut element did not contribute much lift and laminar separation bubbles are present which is typical for all airfoil configurations in this study. Figure 4 compares the aerodynamic performance of the MFS-004 to the DU 00-W-401. The C_l/C_d of this multi-element arrangement at angles of attack greater than $\alpha_{C_l/C_{d_{max}}}$ did not decrease as quickly as the DU 00-W-401 airfoil.

III.B. MFS-104: Second MFS Configuration with Increased Spar Cap Separation

A simple modification of MFS-004 case had the strut element shifted down by 0.10 (10% of the chord) to permit an increase in spar cap separation for increased structural strength and efficiency. The new configuration was designated the MFS-104 and is shown in Fig 5. The airfoil elements of the MFS-104 were identical to those of the MFS-004. The MFS-104 configuration produced a $C_l/C_{d_{max}} = 156.1$ at a $C_l = 2.42$ and $\alpha = 9.7$ deg. Figure 6 presents the C_p and nondimensional velocity distributions, and shows that this downward shift of the strut created higher pressures on the pressure side of the main element relative to the MFS-004 case. As a result more lift was produced by the main element and less lift was produced by the strut element. Additionally, the velocity peak on the suction side of the strut element was reduced in the MFS-104 configuration, and the adverse pressure gradient is weaker. This weaker adverse pressure gradient was due to a combination of the reduced slot effect[9] between the suction side of the strut element and the pressure side of the main element, and the strut being located in an area of reduced streamline curvature. Figure 7 compares the performance of the MFS-104 to the DU 00-W-401. The extra lift produced by the main element resulted in a slightly greater $C_l/C_{d_{max}}$ than the MFS-004, although it appears that beyond $C_l/C_{d_{max}}$, C_l/C_d decreased at a slightly quicker rate with angle of attack than that of the MFS-004. This rate of decrease in C_l/C_d however was still significantly lower than the rate of decrease for the DU 00-W-401 airfoil.

III.C. MFFS-018: Main Element, Flap, Flap, and Strut

The MFFS-018 multi-element configuration benefits from the addition of a second flap to the main element as shown in Fig. 8. This configuration was developed with the goal of further increasing the lift over that of the MFS-004. This second flap resulted in increased camber relative to the MFS-004 case. Figure 9 presents the viscous C_p and nondimensional velocity distributions. The performance of the MFFS-018 is shown in Fig. 10. The MFFS-018 configuration shows a slightly greater lift-to-drag ratio ($C_l/C_{d_{max}} = 158.0$) than the MFS-004 at a lower lift value ($C_l = 2.34$). This configuration appears to be well suited for higher C_l values because it demonstrates the highest $C_l/C_{d_{max}}$ of all the configurations but offers a C_l/C_d at $C_l = 1.7$ that is lower than the MFS-004 and MFS-104. As shown in Fig. 10, the drop off of C_l/C_d beyond $C_l/C_{d_{max}}$ was gentler than that of the DU 00-W-401 airfoil.

III.D. SMFS-004: Slat, Main Element, Flap, and Strut

The SMFS-004 is a derivative of the MFS-003 case and has a leading edge slat added to the main element as shown in Fig. 11. The viscous pressure and nondimensional velocity distributions are presented in Fig. 12. The SMFS-004 configuration produced an $C_l/C_{d_{max}} = 150.4$ at a $C_l = 2.82$ and $\alpha = 15.0$ deg as shown in Fig. 13. For the SMFS-004, Fig. 13 shows the drop off in C_l/C_d of the SMFS-004 beyond $C_l/C_{d_{max}}$ was sharper than that of any of the other multi-element airfoils; however, it still demonstrated a marginal improvement over the sharpness of the drop off in C_l/C_d of the DU 00-W-401 airfoil.

III.E. MSS-001: Main Element, Strut, and Aft Strut

The MSS-001 configuration is shown in Fig. 14. The MSS-001 was derived from placing fairings over the top and bottom spar caps with a third smaller element located aft at mid spacing for torsional rigidity. Due to the large gap between the upper forward and aft elements, no beneficial slot effects[9] were achieved with this design. The MSS-001 configuration produced a $C_l/C_{d_{max}} = 116.9$ at a $C_l = 1.77$ and $\alpha = 14.7$ deg as shown in Fig. 16. The sharpness of the drop off in C_l/C_d beyond $C_l/C_{d_{max}}$ for the MSS-001 multi-element airfoil is gentler than that of the DU 00-W-401 airfoil. Figure 15 shows the C_p and nondimensional velocity distributions for the MSS-001.

III.F. MSS-102: Second MSS Configuration with a Larger Aft Strut

Attempting to improve on the MSS-001 case, the MSS-102 configuration evolved to have a larger aft airfoil section. As depicted in Fig. 17, this larger aft airfoil reduced the size of the gap between the upper forward and aft elements. This decreased gap allowed the aft element to behave more like a flap[9] than a nearly isolated airfoil as in the MSS-001 configuration. This increased multi-element effect is reflected in the performance comparison of Fig. 19 which shows that the MSS-102 configuration produced a $C_l/C_{d_{max}} = 121.1$ at a $C_l = 2.01$ and $\alpha = 14.9$ deg. Figure 18 depicts the C_p and nondimensional velocity distributions. The sharpness of the drop off in C_l/C_d beyond $C_l/C_{d_{max}}$ for the MSS-102 multi-element airfoil was gentler than that of the DU 00-W-401 airfoil.

III.G. MFSF-006: Main Element with Flap, and Strut with Flap

The MFSF-006 configuration was developed from an original layout that would have encompassed the DU 00-W-401 airfoil with a rectangular box. Like the aft element of the MSS case, the goal behind the original layout was resistance to torsion. It soon became apparent that a true box arrangement, best described as two biplanes arranged in tandem, would not take advantage of the benefits of multi-element configurations. For this reason, the MFSF configuration evolved into one with a pair of flapped airfoil elements, with the flapped elements being the main and strut elements. The MFSF-006 geometry is shown in Fig. 20. The MFSF-006 configuration produced a $C_l/C_{d_{max}} = 128.4$ at a $C_l = 2.99$ and $\alpha = 12.0$ deg. Figure 21 presents the viscous C_p and inviscid velocity distributions, and Fig. 22 compares the aerodynamic performance of the MFSF-006 to that of the DU 00-W-401 airfoil. As shown in Fig. 22, the MFSF-006 multi-element airfoil exhibited a gentler drop off in C_l/C_d beyond $C_l/C_{d_{max}}$ than the DU 00-W-401.

IV. Discussion

These multi-element blade root airfoil results appear very promising, but their effectiveness may be evaluated only through further research involving a higher fidelity viscous analysis and wind tunnel testing. Additionally, the task of incorporating multi-element airfoils into a wind turbine blade design must be addressed. Once a multi-element airfoil configuration is selected for the blade root, the configuration must be used to generate a family of airfoils that follows a specified spanwise C_l distribution and is able to interface with a conventional single-element blade airfoil. The optimal spanwise blade location at which to switch from a multi-element to a single-element arrangement and the resulting wind turbine performance benefits must also be studied. This study of the incorporation and performance benefits of multi-element airfoils into a wind turbine blade design will be the subject of a further work. The viability of an MFS-style arrangement with its higher design lift coefficient versus an MSS-style design with its wind turbine blade operating C_l being located much closer to the conditions for $C_l/C_{d_{max}}$ also must still be investigated. To shed some light into determining a multi-element airfoil design C_l, early studies into a blade design incorporating multi-element airfoils on the inboard section suggest that the blade root should have a design C_l of around 1.7 so as to not grossly alter the structural requirements of the blade. This design C_l will also maintain a reasonable blade chord distribution. For these reasons, the performance benefits of each of the seven multi-element arrangements at $C_l = 1.7$ are presented in Table 3. The SMFS-004 and MFSF-006 multi-element airfoil configurations were unable to yield a converged solution for $C_l = 1.7$ due to their significantly higher design C_l (see Table 2).

Table 3. Multi-Element Airfoil Performance Summary ($C_l = 1.7$)

Airfoil	C_l/C_d at $C_l = 1.7$	% Increase in C_l/C_d
DU 00-W-401	82.9 ($C_l = 1.04$)	–
MFS-004	133.1	60.6
MFS-104	133.2	60.7
MFFS-018	130.0	56.8
SMFS-004	n/a	n/a
MSS-001	116.4	40.4
MSS-102	117.0	41.3
MFSF-006	n/a	n/a

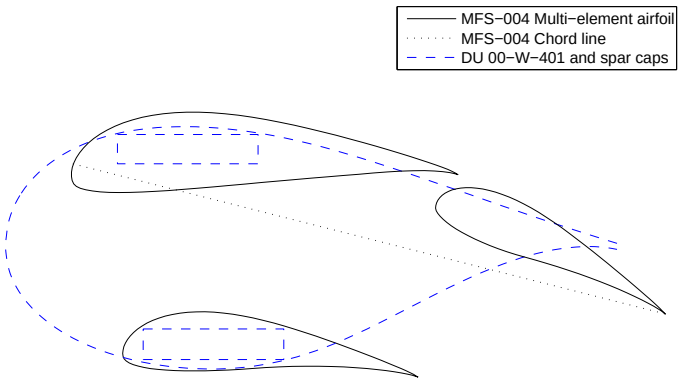

Figure 2. MFS-004 multi-element airfoil geometry.

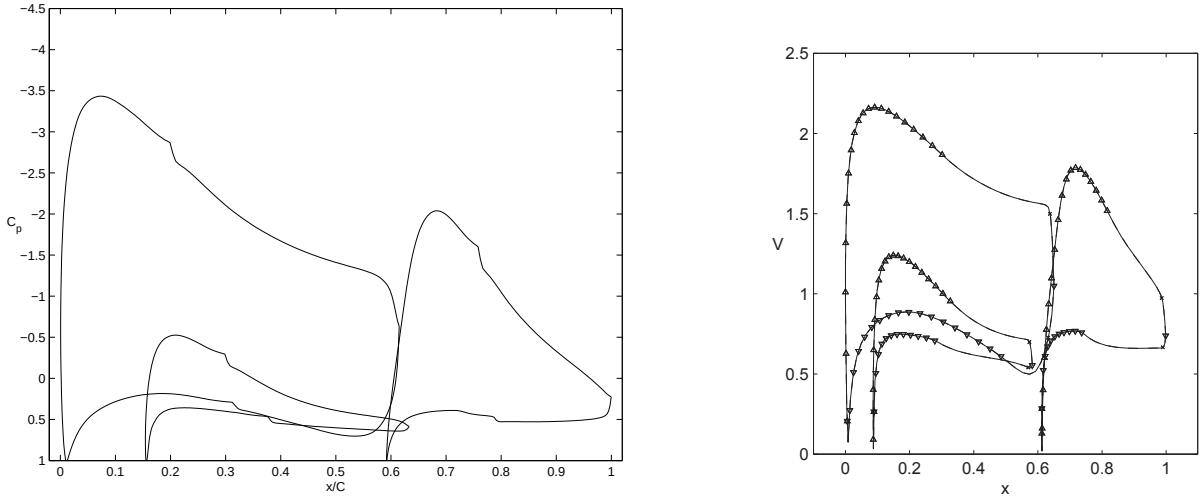

b) Pressure distributions at $Re = 3.0 \times 10^6$ **a) Inviscid velocity distributions**

Figure 3. MFS-004 viscous pressure and inviscid velocity distributions at $C_l/C_{d_{max}}$ ($\alpha = 10.0$ deg, $C_l = 2.42$).

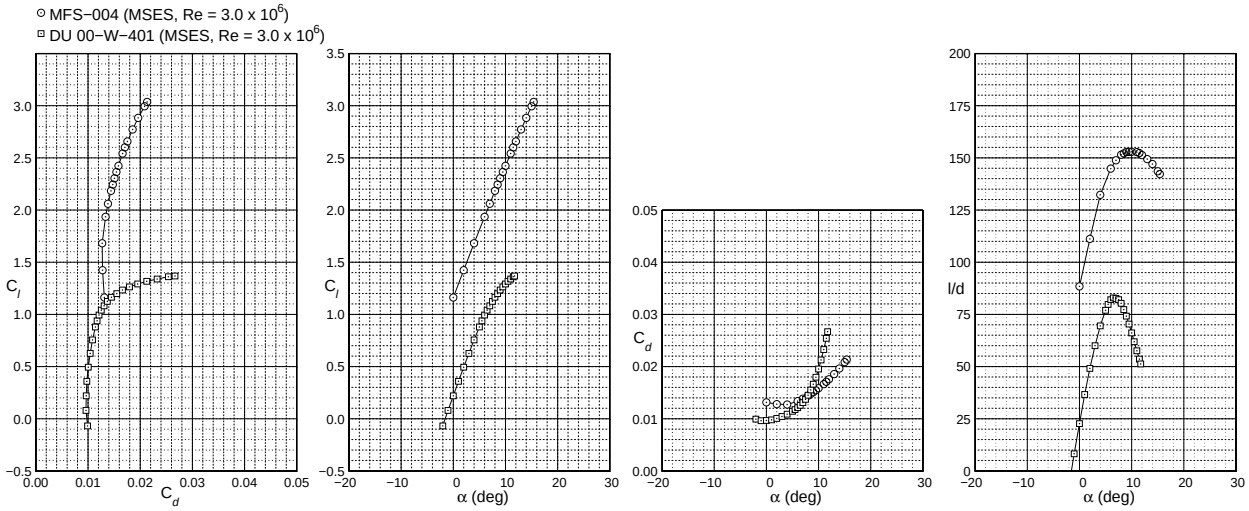

Figure 4. MFS-004 lift and drag performance comparisons to the DU 00-W-401 at $Re = 3.0 \times 10^6$.

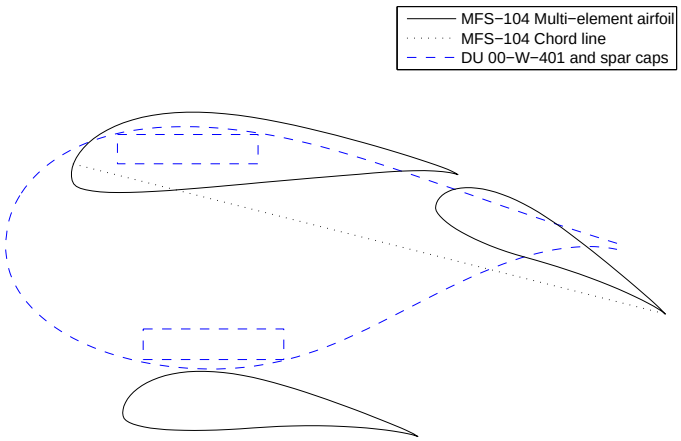

Figure 5. MFS-104 multi-element airfoil geometry.

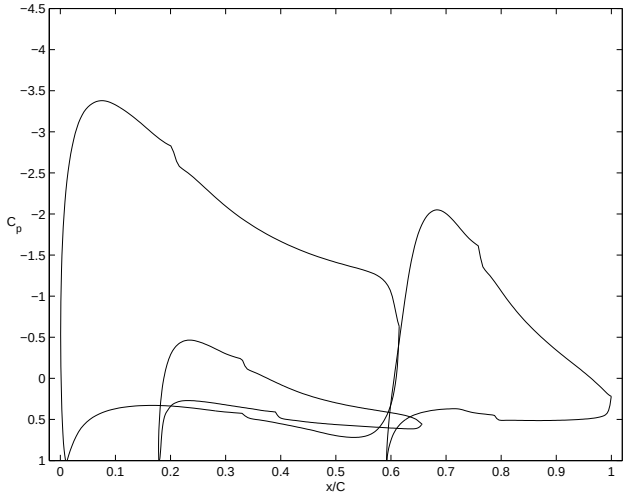

a) Pressure distributions at $Re = 3.0 \times 10^6$

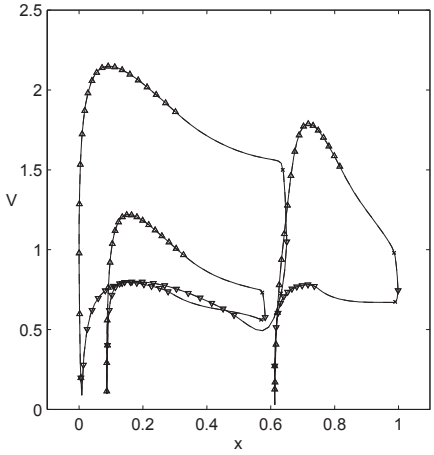

b) Inviscid velocity distributions

Figure 6. MFS-104 viscous pressure and inviscid velocity distributions at $C_l/C_{d_{max}}$ ($\alpha = 9.7$ deg, $C_l = 2.42$).

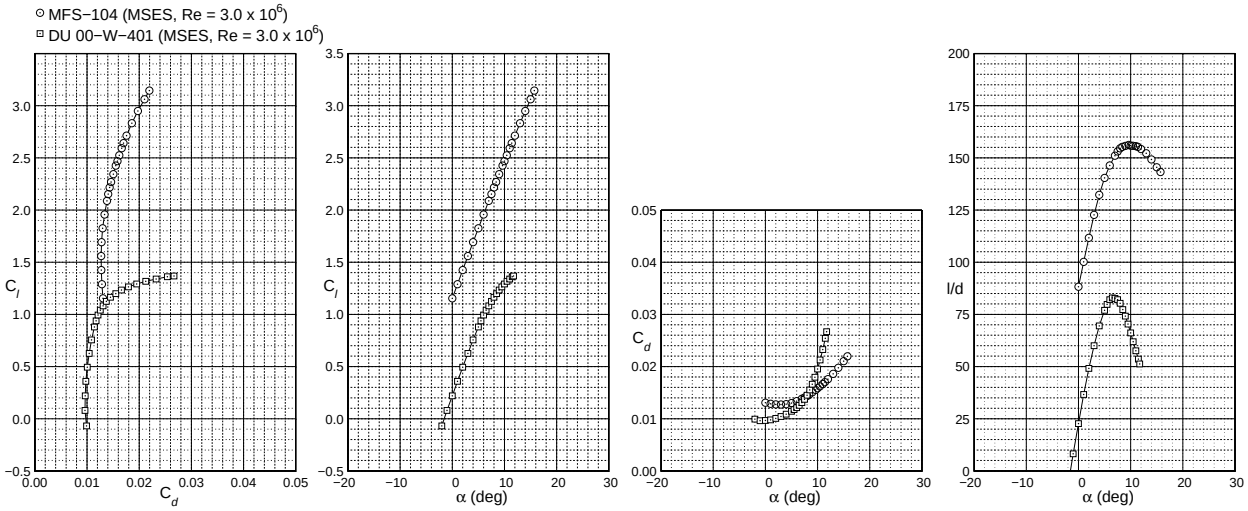

Figure 7. MFS-104 lift and drag performance comparisons to the DU 00-W-401 at $Re = 3.0 \times 10^6$.

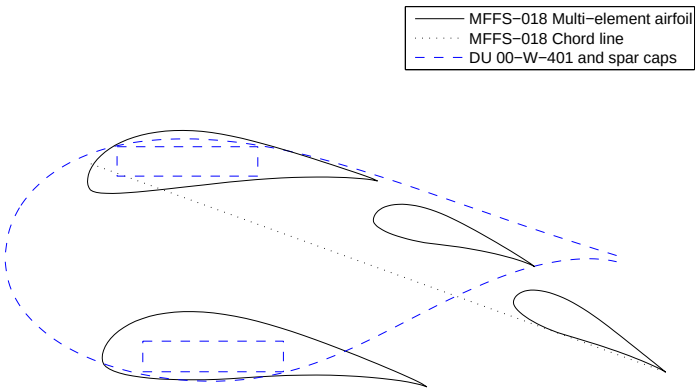

Figure 8. MFFS-018 multi-element airfoil geometry.

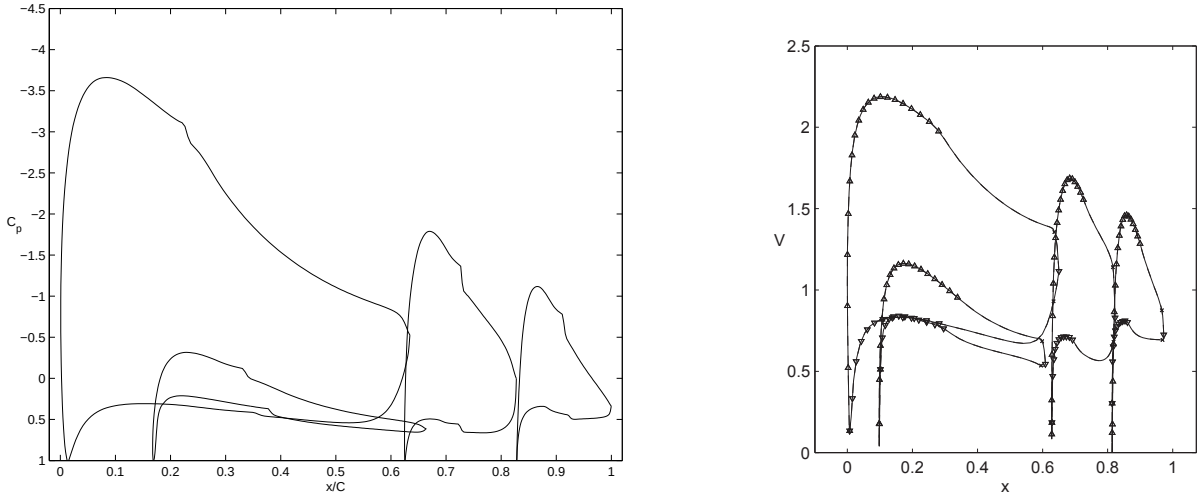

a) Pressure distributions at $Re = 3.0 \times 10^6$

b) Inviscid velocity distributions

Figure 9. MFFS-018 viscous pressure and inviscid velocity distributions at $C_l/C_{d_{max}}$ ($\alpha = 12.9$ deg, $C_l = 2.34$).

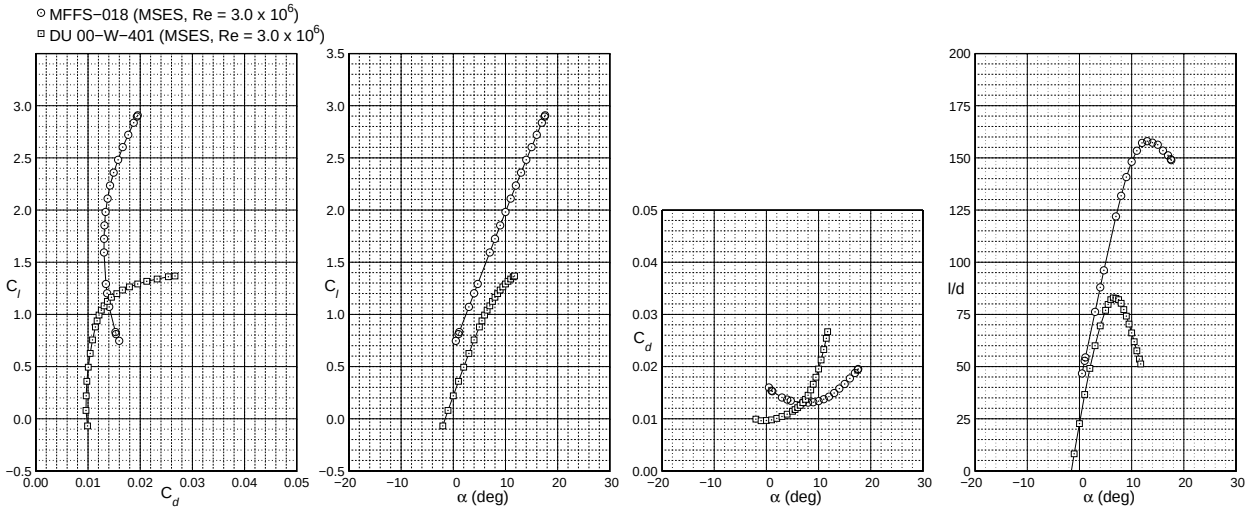

Figure 10. MFFS-018 lift and drag performance comparisons to the DU 00-W-401 at $Re = 3.0 \times 10^6$.

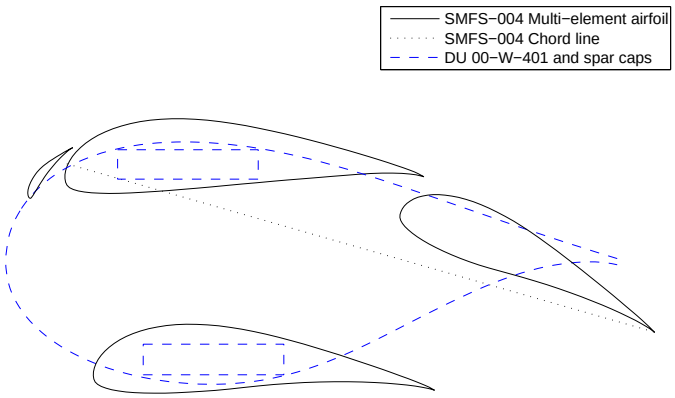

Figure 11. SMFS-004 multi-element airfoil geometry.

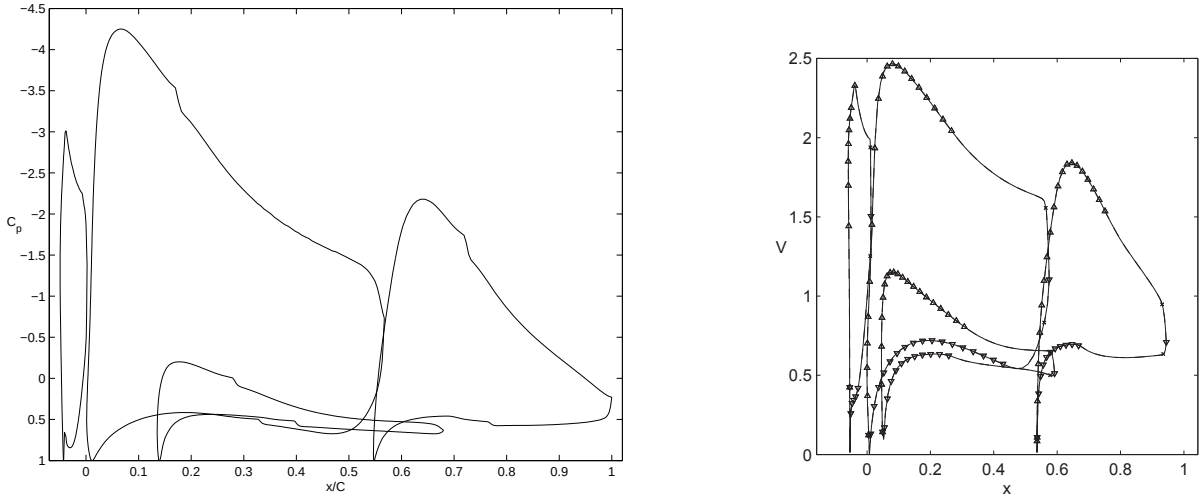

a) Pressure distributions at $Re = 3.0 \times 10^6$

b) Inviscid velocity distributions

Figure 12. SMFS-004 viscous pressure and inviscid velocity distributions at $C_l/C_{d_{max}}$ ($\alpha = 15.0$ deg, $C_l = 2.82$).

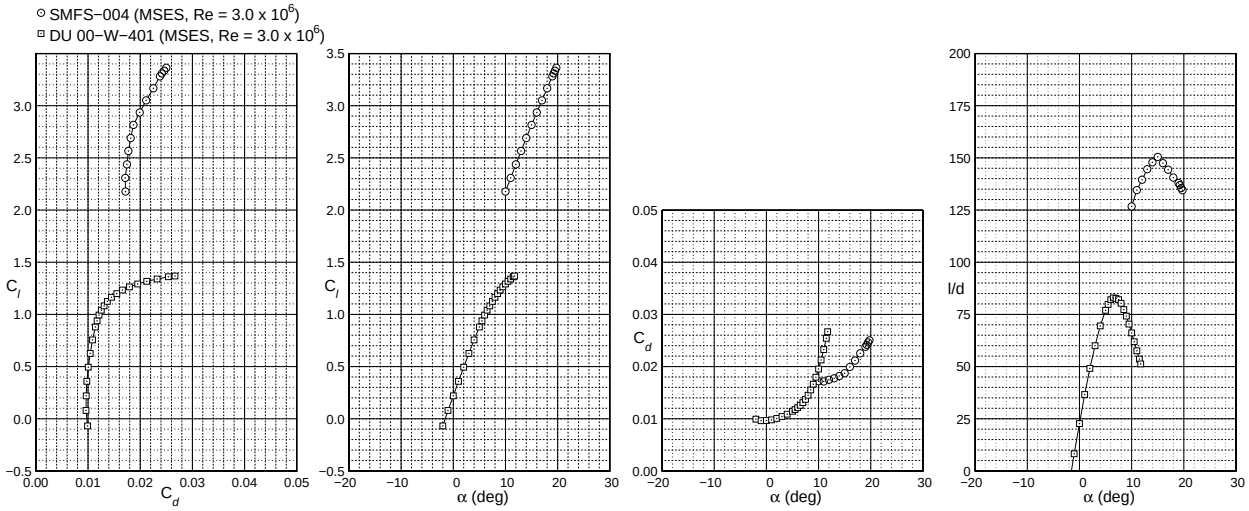

Figure 13. SMFS-004 lift and drag performance comparisons to the DU 00-W-401 at $Re = 3.0 \times 10^6$.

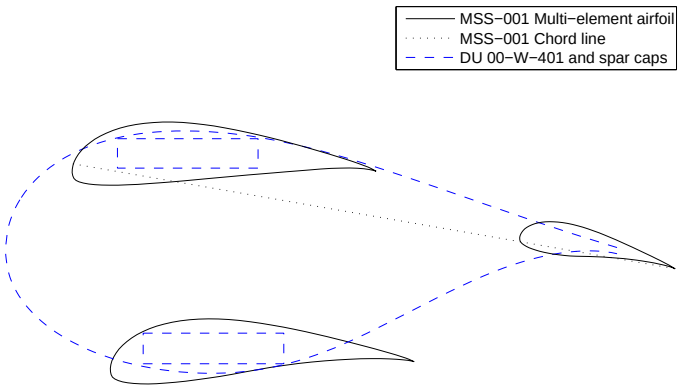

Figure 14. MSS-001 multi-element airfoil geometry.

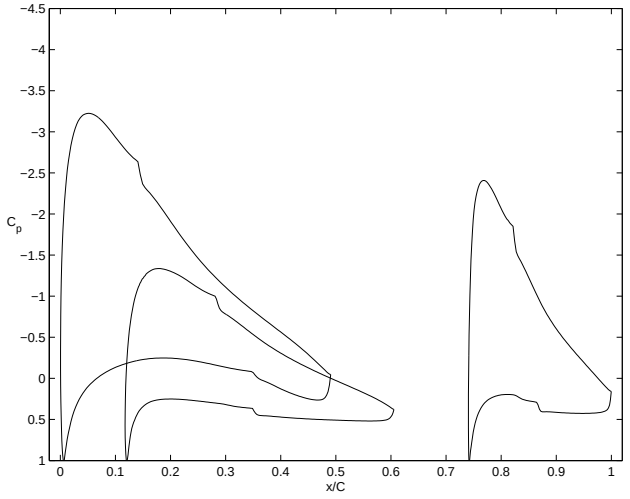

a) Pressure distributions at $Re = 3.0 \times 10^6$

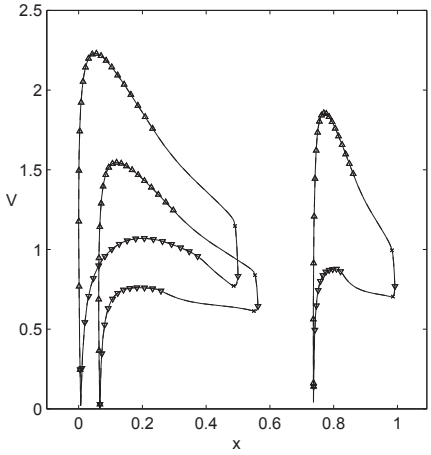

b) Inviscid velocity distributions

Figure 15. MSS-001 viscous pressure and inviscid velocity distributions at $C_l/C_{d_{max}}$ ($\alpha = 14.7$ deg, $C_l = 1.77$).

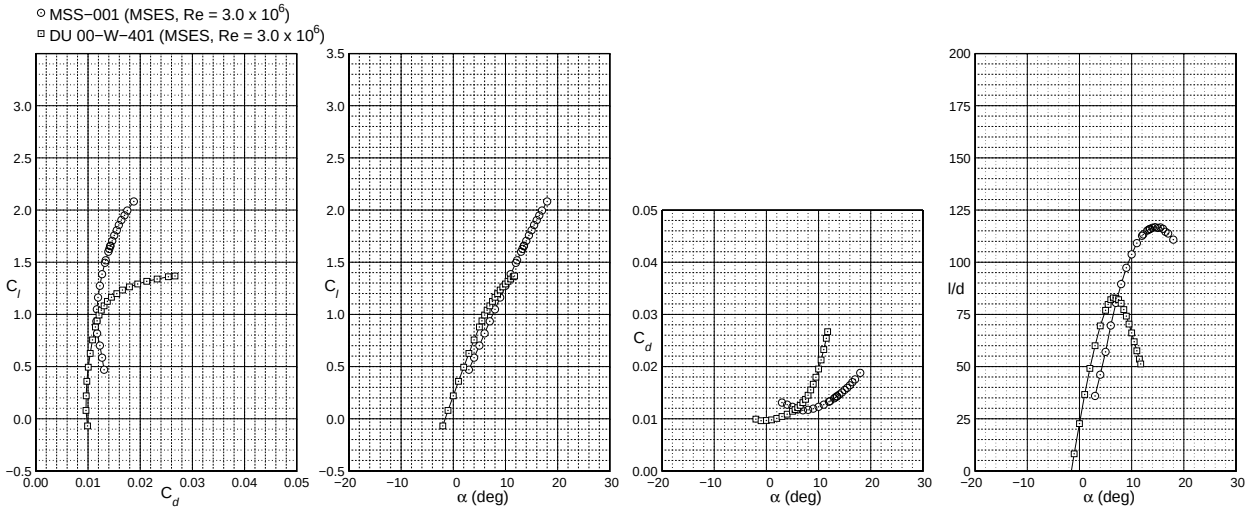

Figure 16. MSS-001 lift and drag performance comparisons to the DU 00-W-401 at $Re = 3.0 \times 10^6$.

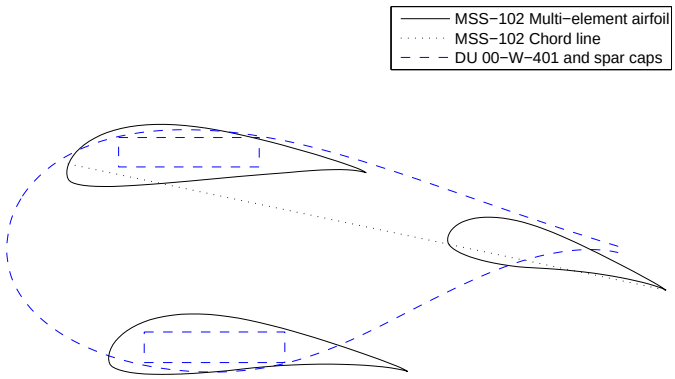

Figure 17. MSS-102 multi-element airfoil geometry.

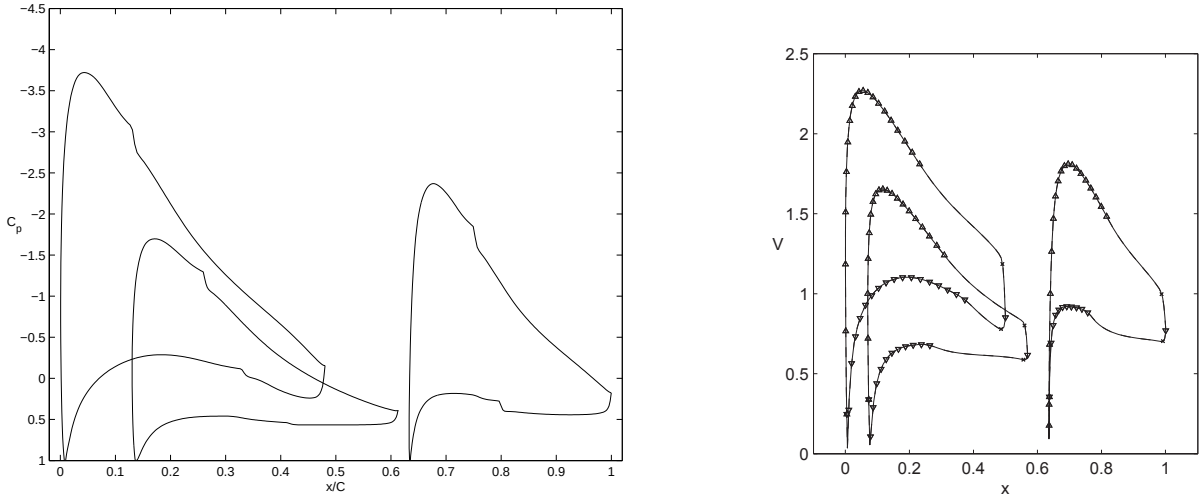

a) Pressure distributions at $Re = 3.0 \times 10^6$

b) Inviscid velocity distributions

Figure 18. MSS-102 viscous pressure and inviscid velocity distributions at $C_l/C_{d_{max}}$ ($\alpha = 14.9$ deg, $C_l = 2.01$).

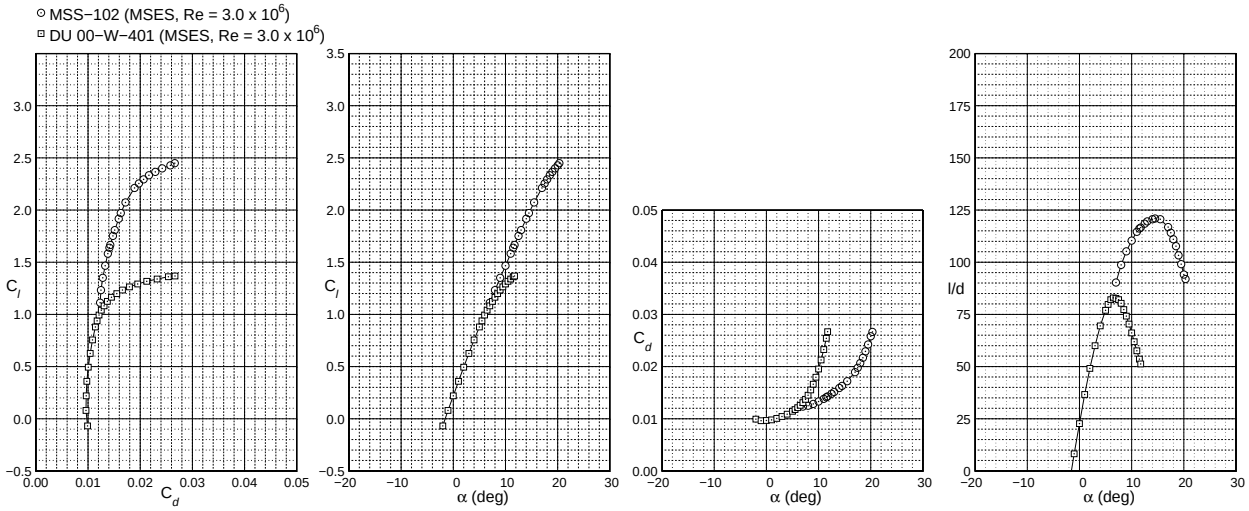

Figure 19. MSS-102 lift and drag performance comparisons to the DU 00-W-401 at $Re = 3.0 \times 10^6$.

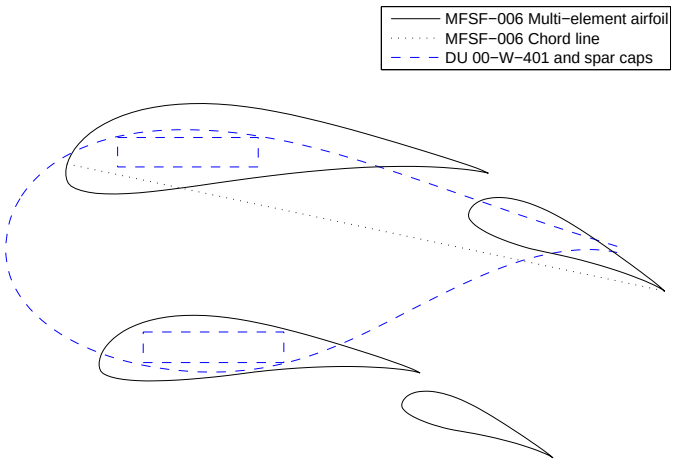

Figure 20. MFSF-006 multi-element airfoil geometry.

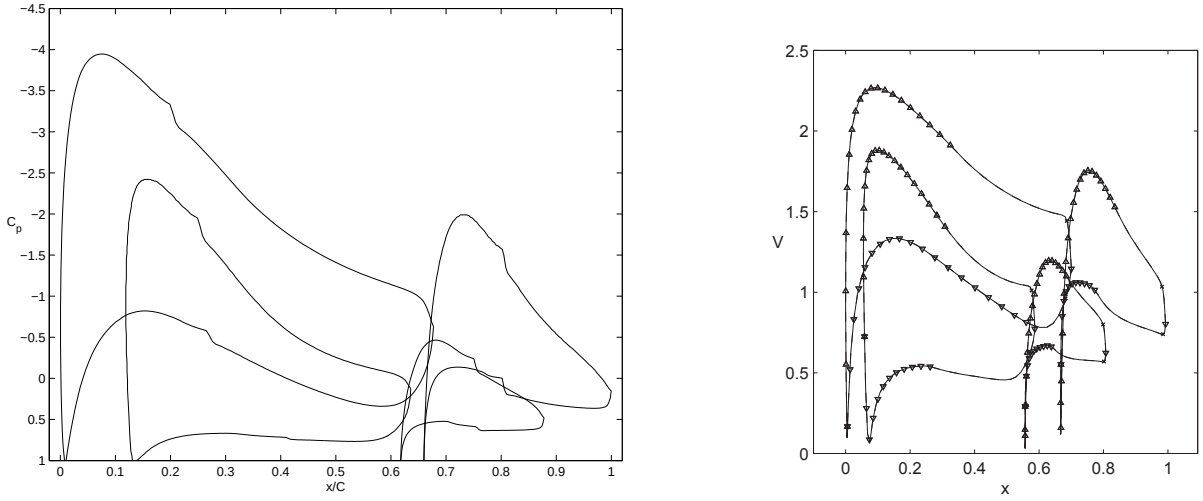

a) Pressure distributions at $Re = 3.0 \times 10^6$

b) Inviscid velocity distributions

Figure 21. MFSF-006 viscous pressure and inviscid velocity distributions at $C_l/C_{d_{max}}$ ($\alpha = 12.0$ deg, $C_l = 2.99$).

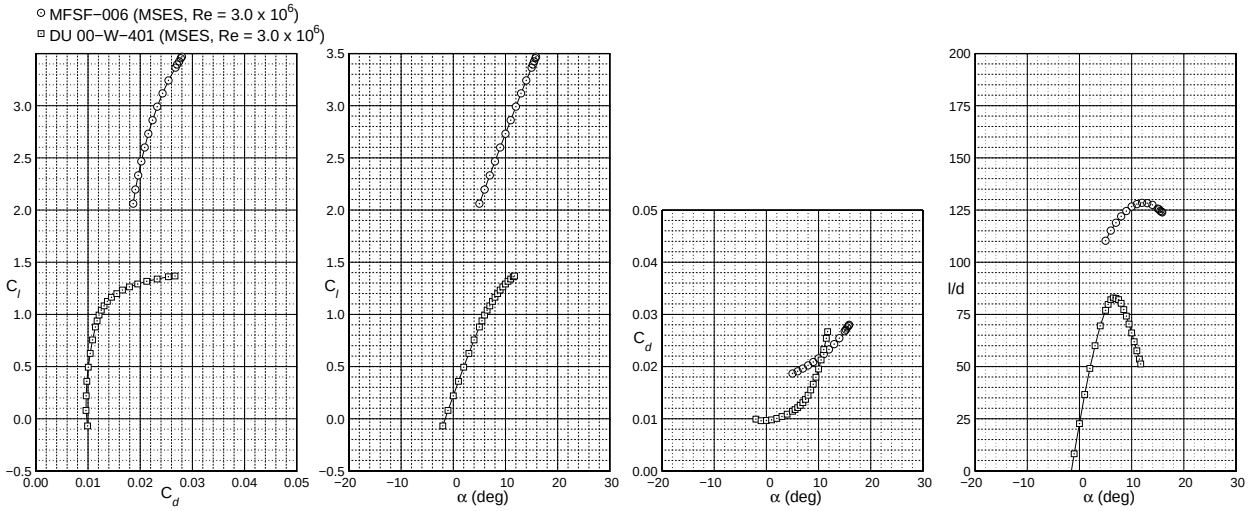

Figure 22. MFSF-006 lift and drag performance comparisons to the DU 00-W-401 at $Re = 3.0 \times 10^6$.

V. Conclusions

Aerodynamically, these seven multi-element airfoil configurations in many respects are superior to typical thick root airfoil sections of modern megawatt-scale wind turbines. When compared with a traditional section, these multi-element configurations are capable of producing much higher maximum lift coefficients, with C_l values of 3.0 and higher compared with the $C_{l_{max}} = 1.04$ for the 40.1% thick DU 00-W-401 airfoil. Moreover, these multi-element airfoil configurations produce much higher lift-to-drag ratios on account of both higher lift and much lower drag, with increases of between 40% and 88% in $C_l/C_{d_{max}}$. As shown in Table 2, the MFFS-018 multi-element configuration produced the greatest percent gain in $C_l/C_{d_{max}}$, with a 90.5% increase over the DU 00-W-401. At $C_l = 1.7$ the MFS-104 multi-element configurations produced the greatest percent gain in C_l/C_d with a 60.7% increase over the DU 00-W-401 airfoil. The $C_l = 1.7$ was selected as a realistic value for the inboard section of a wind turbine blade; significantly larger C_l values would greatly exceed current blade structural limits. Clearly exhibiting that they did not fully realize the multi-element slot effect,[9] the MSS-001 and MSS-102 configurations were able to offer $C_l/C_{d_{max}}$ improvements of 41.0% and 46.1%, respectively. Due to both MSS arrangements having a lower design C_l, the change from $C_l/C_{d_{max}}$ to C_l/C_d at $C_l = 1.7$ was much less, yielding a percent increase of 40.4% and 41.3% at the lower C_l. As demonstrated by the SMFS case, the addition of a slat results in an increase in the $C_l/C_{d_{max}}$ value of a multi-element arrangement, but this comes at the cost of a sharper drop off in C_l/C_d above $C_l/C_{d_{max}}$ when compared with a non-slatted multi-element arrangement. By moving the strut element farther below the main and flap elements, as was the case in the MFS-104 multi-element airfoil, the $C_l/C_{d_{max}}$ value may be increased as a larger amount of lift is generated by the main element. As a result of the improved aerodynamic performance, the potential for better start-up performance exists due to higher start-up torque from higher lift airfoils and also increased blade efficiency from more closely matched ideal operating conditions along the blade. Altogether, these aerodynamic advantages are expected to increase the efficiency of the wind turbines through both increased energy production and reductions in blade material and mass, with an ultimate result of a lower cost of energy. For very large wind turbines, the use of a multi-element airfoil configuration in lieu of an otherwise extremely large blade root section would make transport over land more viable by allowing piecewise assembly on site.

VI. Acknowledgments

The authors would like to thank GE Energy for their financial support of this investigation.

References

[1]Griffin, D. A. and Ashwill, T. D., "Alternative Composite Materials for Megawatt-Scale Wind Turbine Blades: Design Considerations and Recommended Testing," *Proceedings of the 41st Aerospace Sciences Meeting and Exhibit*, AIAA Paper 2003-696, 2003.

[2]Selig, M. S. and Maughmer, M. D., "Multipoint Inverse Airfoil Design Method Based on Conformal Mapping," *AIAA Journal*, Vol. 30, No. 5, 1992, pp. 1162–1170.

[3]Selig, M. S. and Maughmer, M. D., "Generalized Multipoint Inverse Airfoil Design," *AIAA Journal*, Vol. 30, No. 11, 1992, pp. 2618–2625.

[4]Gopalaranthnam, A. and Selig, M. S., "Low-Speed Natural-Laminar-Flow Airfoils: Case Study in Inverse Design," *AIAA Journal of Aircraft*, Vol. 38, No. 1, 2001, pp. 57–63.

[5]Drela, M. and Giles, M. B., "Viscous-Inviscid Analysis of Transonic and Low Reynolds Number Airfoils," *AIAA Journal*, Vol. 25, No. 10, 1987, pp. 1347–1355.

[6]Drela, M., "Design and Optimization Method for Multi-Element Airfoils," *Proceedings of the AIAA/AHS/ASEE Aerospace Design Conference*, AIAA Paper 93-0960, 1993.

[7]Drela, M., "A User's Guide to MSES 3.05," *MIT Department of Aeronautics and Astronautics*, July, 2007.

[8]van Rooij, R. and Timmer, W., "Roughness Sensitivity Considerations for Thick Rotor Blade Airfoils," *Proceedings of the 41st Aerospace Sciences Meeting and Exhibit*, AIAA Paper 2003-350, 2003.

[9]Smith, A. M. O., "High-Lift Aerodynamics," *AIAA Journal of Aircraft*, Vol. 12, No. 6, 1975, pp. 501–530.